

Research on the transition dynamics and linear (nonlinear) optical properties of mCherry

Yuanjin Wang,[†] Gaoshang Li,[†] Jin Dai,^{*,†} Xubiao Peng,^{*,†} and Qing Zhao^{*,†,‡}

[†]*Center for Quantum Technology Research, Key Laboratory of Advanced Optoelectronic Quantum Architecture and Measurements (MOE), School of Physics, Beijing Institute of Technology, Beijing, China*

[‡]*Beijing Academy of Quantum Information Sciences, Beijing 100193, China*

E-mail: jindai@bit.edu.cn; xubiaopeng@bit.edu.cn; qzhaoyuping@bit.edu.cn

Abstract

In this study, we explore the electron transition mechanism and optical properties of the popular red fluorescent protein mCherry. By examining the charge transfer spectrum and combining it with the mCherry hole-electron distribution, we identify that the charge transfer between the phenolate and imidazolinone loops significantly contributes to the absorption spectrum. Quantitative analysis of charge transfer shows that, overall, the electrons are transferred to the C16 atom in the middle of phenolate and the imidazolinone loops during absorption. We speculate that C16 may also absorb protons to enable the photoconversion of mCherry in the excited state, similar to the blinking mechanism of IrisFP. In addition, we further investigated the optical properties of mcherry in the external field by polarizability (hyperpolarizability), showing the anisotropy of the polarization, the first hyperpolarization and the second hyperpolarization by unit spherical representation. Our results suggest that significant polarization and second hyperpolarizability occur when the field direction and electron transfer direction are aligned. We also analyzed the polarizability and first hyperpolarizabilities for different external fields. The polarizability mutated when the external field satisfies the $S_{0,min} \rightarrow S_1$ transition. Finally, the study of the first hyperpolarizability shows that adjusting the appropriate

field can lead to a linear photoelectric effect or second harmonic generation of mCherry. These studies have certain reference values for various red fluorescent protein correlation simulations and experiments because of the similarity of the red fluorescent protein.

Introduction

Fluorescent proteins (FPs), derived from green fluorescent proteins found in the jellyfish *Aequorea victoria*,¹ can be engineered to respond to various biological events and signals, rendering them valuable for various biological tissues and organisms while rarely causing photodynamic toxicity.²

Decades of research have resulted in a family of FPs that span the entire visible spectrum, leading to the development of powerful fluorescent probes and revealing the complexity and application value of the photophysical properties of proteins.³⁻⁹ In bioimaging and sensing, FPs and their derived biosensors make it possible to probe the location, activities, or interactions of molecules from the subcellular to multicellular scales.¹⁰ Fluorescence imaging technology is ideal for measuring the pathophysiological microenvironment measurement,¹¹ and fluorescent protein nanothermometers have the capability of accurately targeting to organelles and genetically encode.¹² Tumour-targeted fluorescence-guided surgery enables

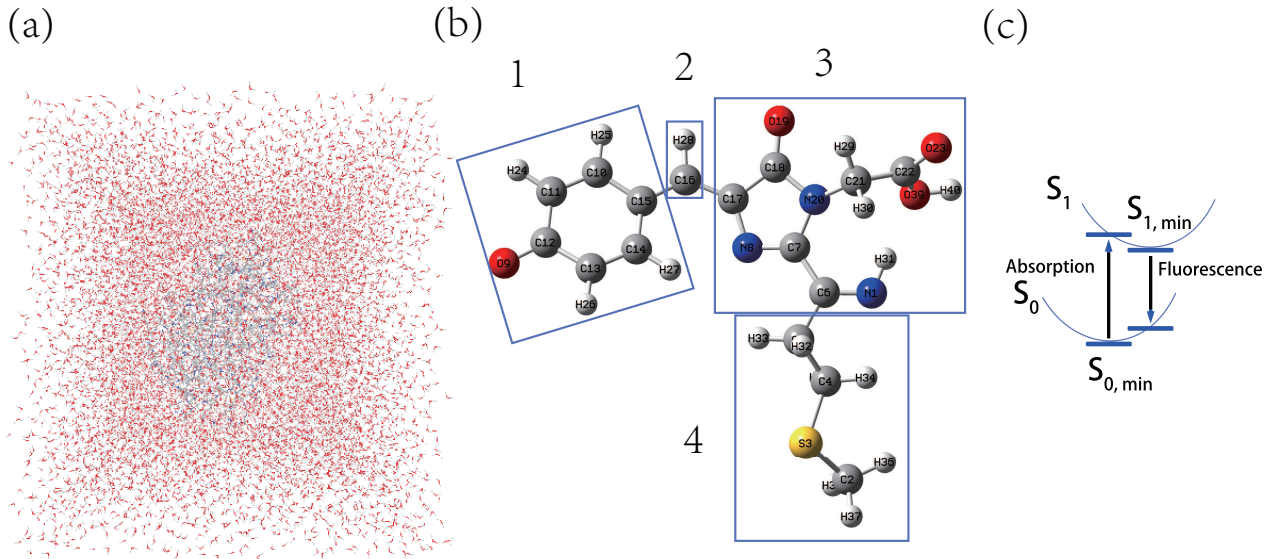


Figure 1: (a) Crystal structure of mCherry. Protein in the middle and water molecules in the periphery. (b) Chromophore. Gray, red, white, blue, and yellow colors refer to the C , O , H , N and S atoms, respectively. The chromophore was divided into four regions for analysis. (c) Absorption and fluorescence process diagram. S_0 means that the molecule is in the ground state, and $S_{0,min}$ is the minimum point of the ground state. The first excited state and its minimum are S_1 and $S_{1,min}$, respectively. $S_{0,min} \rightarrow S_1$ corresponds to the absorption process, while $S_{1,min} \rightarrow S_0$ is the fluorescence process.

the visualization of solid tumors,¹³ while fluorescence lifetime imaging and Förster resonance energy transfer has been coupled with multiphoton microscopy for *in vivo* dynamic imaging.¹⁴ Many photoinduced reactions of FPs, such as photoisomerization, excited-state proton transfer, photooxidation/photoreduction, are initiated by electron transfer.¹⁵ The reversible photoconversion characteristic of fluorescent proteins to switch back and forth between fluorescent and nonfluorescent states is highly significant to the development of advanced fluorescence imaging and biotechnology based on their photophysical properties.^{16–18} Engineering FPs to switch between dark and detectable states enables to image structures with spatial resolution beyond Abbe’s diffraction limit.¹⁹ Dynamic fluorescence can adjust surface patterns through external stimulation, which is highly valuable in the fields of smart displays, information storage, and anticounterfeiting.^{20–24}

Red fluorescent proteins (RFPs) have low scattering and large penetration depth in the

red to near-infrared region, making them advantageous in deep-tissue imaging of live animals owing to their longer excitation and emission wavelengths.^{3,25} For instance, the bright red fluorophore mRuby3 can be used to design a voltage-activated red neuronal activity monitor, extending the application of genetically encoded voltage indicators in high-speed multispectral imaging and opening the door to high-speed multispectral functional imaging *in vivo*.²⁶ The energy of the excited state of RFPs strongly correlates with the magnetic dipole moment, which can be used to adjust the spectrum of markers in *in vivo* imaging.²⁷

Although mCherry has low fluorescence quantum yield, it is a popular red fluorescent protein, the lineage of which can be traced to the naturally occurring tetramer DsRed.²⁸ However, naturally occurring RFPs occur in dimeric or tetrameric form, both of which tend to oligomerize and are unsuitable for fusion tagging.^{29–32} Several novel mutant monomeric variants known as mFruits have been designed to address this issue; among the designed variants,

mCherry, mOrange, and mStrawberry are the most promising.^{28,33,34} Compared to its progenitor, mCherry has the advantages of a favorable red-shift of absorption and emission spectra, higher expression and fast chromophore maturation, and lower phototoxicity.³⁵ Unfortunately, the fluorescence quantum yield of mcherry is only one-third, rendering it substantially dimmer than DsRed.^{28,36} The second-order nonlinear optical response (β) of fluorescent proteins including mCherry can be measured via Hyper-Rayleigh Scattering and is suitable for second-harmonic imaging microscopy.³⁷ RFPs with a common origin are similar, and their transition mechanism in absorption and emission is intriguing. However, related studies on this photoinduced reaction are relatively few. Consequently, we posit that studying the transition mechanism of mCherry in detail could provide some references for experiments related to mCherry and other RFPs.

In this study, we used the QM/MM method to simulate the absorption process of mcherry, and we analyzed the calculated wave function using Multiwfn (Version 3.8(dev))³⁸ software to investigate the transition mechanism and optical properties of mCherry. The absorption process involves molecular transition from the ground state minimum ($S_{0,min}$) to the excited state ($S_i, i = 1, 2, 3 \dots$); we consider only the $S_{0,min} \rightarrow S_1$ transition with the largest contribution to the mCherry absorption spectrum. Using Multiwfn, we introduced hole-electron analysis to study the transition mechanism of mCherry. First, we observe the hole-electron distribution³⁹ of the excited state, and combined with the charge transfer spectrum⁴⁰ of mCherry, we investigate the influence of the charge transfer within the chromophore on the absorption spectrum. Second, we quantitatively analyzed charge transfer during absorption using the interfragment charge transfer module⁴¹ of Multiwfn and plotted a heat map. Additionally, we focus on the polarization and hyperpolarization calculated by the complete state summation method,⁴² showing the polarizability, the first and second hyperpolarizations in all directions using the unit spherical representation.^{43,44} Finally, we stud-

ied the polarizability and the first hyperpolarization under different external fields and analyzed the linear and nonlinear optical properties of mCherry.

Models and methods

Herein, we used ORCA (Version 5.0.3)⁴⁵ software for QM/MM calculation and Multiwfn³⁸ software for data analysis. To prepare for the analysis, we obtained the mCherry crystal structure file (code 2H5Q)⁴⁶ from the Protein Data Bank. Then, we used VMD⁴⁷ software to cover it with a layer of water molecules 15Å thick (Fig.1(a)), and generate a protein structure file (PSF), in which residue glu215 was adjusted to a protonation state.

Using Avogadro,⁴⁸ we individually added H atoms to the chromophore and additionally appended OH^- and H^+ ions at the interface to compensate for the effects of bond breakage. As shown in Fig.1(b), the three extra attached atoms are $O39$, $H40$, and $H31$ at the right end. To investigate the role of phenolate and imidazolinone, we referred to the three-state adiabatic model^{49,50} to divide the chromophore into four regions. Region 1 comprises the phenolate ring, Region 3 includes the imidazolinone ring and partially surrounding atoms, Region 2 comprises the phenolate ring and the imidazolinone ring middle region, and the remaining parts are included in Region 4. The PSF file was then transformed into an ORCA force field file, and the force field file of the chromophore was generated directly in the ORCA software using the `orca_mm` module. Subsequently, the mCherry was pre-optimized using the LBFGS optimizer (keyword "L-Opt") in ORCA.

To facilitate the analysis, we performed a geometric manipulation of the molecule using Multiwfn. In order, making the $C - H$ bond of region 2 parallel to the Y -axis, selecting the heavy atom center of region 1 – 3 as the origin of coordinates, and adjusting the phenolate ring of region 1 parallel to the $x - y$ plane.

Next, we initiated the QM/MM calculation using ORCA software. As shown in Fig.1(c), we regard $S_{0,min} \rightarrow S_1$ directly as the ab-

sorption process, while the fluorescence process is $S_{1,min} \rightarrow S_0$. The structure optimization level was CAM-B3LYP(D3)/cc-pVDZ, where the QM region contained only the chromophore, and the active region included all atoms within 12Å of the chromophore. We then selected the higher level DSD-PBEP86(D3)/may-cc-pV(T+d)Z to perform TDDFT calculations and imported the results into Multiwfn for spectra drawing and various analyses.

We analyze the linear (nonlinear) optical characteristics of mCherry in different external fields by polarization (hyperpolarization). In Multiwfn, the complete state summation method was used to calculate polarization and hyperpolarizability.⁴² The Taylor expansion of the system energy E relative to the uniform external field F is given as⁵¹

$$E(F) = E(0) - \mu_0 F - \frac{1}{2} \alpha F^2 - \frac{1}{6} \beta F^3 - \frac{1}{24} \gamma F^4 \dots$$

where μ_0 is called the permanent dipole moment, α is the polarizability (linear optical coefficient), β is the first hyperpolarizability (second-order nonlinear optical coefficient) and γ is the second hyperpolarizability (third-order nonlinear optical coefficients), which satisfies

$$\begin{aligned} \mu_0 &= - \left. \frac{\partial E}{\partial F} \right|_{F=0}, \alpha = - \left. \frac{\partial^2 E}{\partial F^2} \right|_{F=0}, \\ \beta &= - \left. \frac{\partial^3 E}{\partial F^3} \right|_{F=0}, \gamma = - \left. \frac{\partial^4 E}{\partial F^4} \right|_{F=0}. \end{aligned}$$

In addition, the total dipole moment $\mu = -\frac{\partial E}{\partial F}$ can be expressed as

$$\mu = \mu_0 + \underbrace{\alpha F}_{\mu_1} + \underbrace{(1/2)\beta F^2}_{\mu_2} + \underbrace{(1/6)\gamma F^3}_{\mu_3} + \dots$$

where $\mu_i (i = 1, 2, 3)$ is called the induced dipole moment. Assuming that the external field per unit strength is used, the polarizability (hyperpolarizability) under the electrostatic field can measure the change in the molecule-induced dipole moment. Generally, molecules with stronger polarizability tend to have larger molecular volumes.^{52,53}

Results and discussion

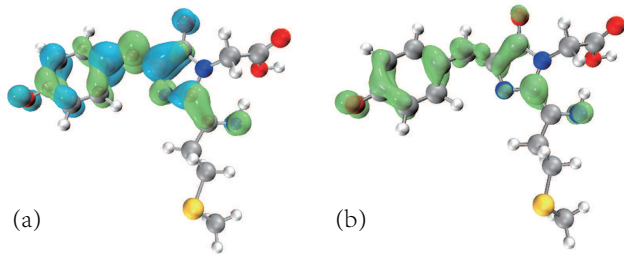


Figure 2: (a) Hole-electron distribution in the S_1 state. The blue surface represents the hole distribution, whereas the green surface represents the electron distribution. (b) Function Sr distribution diagram. The smooth green surface reflects the hole-electron overlap region.

Hole-Electron Distribution. Fig.2(a) shows the hole-electron distribution in the S_1 state of mCherry. It is apparent that the holes and electrons are mainly distributed around the phenolate ring and the imidazolinone ring. Based on Fig.1(b), electron transfer exclusively occurs in Regions 1 – 3 and no hole-electron distribution in Region 4. In the absorption process, the molecule transitions from the ground state to the first excited state, loses electrons in the region of the blue grid surface and obtains electrons in the region of the green grid surface, eventually leading to massive electron transfer inside Regions 1 – 3. In addition, we have attempted to expand the QM region, but the final hole-electron distribution is not significantly different.

Fig.2(b) indicates the region where the electrons and holes significantly overlap. As can be clearly observed therein, the electrons and holes overlapped very heavily. Moreover, based on the output of Multiwfn, the centroid distance between the hole and the electron is only 0.405Å, which is less than half of the $C - C$ single bond (about 1.55 Å⁵⁴). From the high overlap of holes and electrons, we infer that the $S_{0,min} \rightarrow S_1$ transition is accompanied by a large transition electric dipole moment, corresponding to a large oscillator intensity, eventually producing a strong absorption peak in the absorption spectrum.⁵⁵

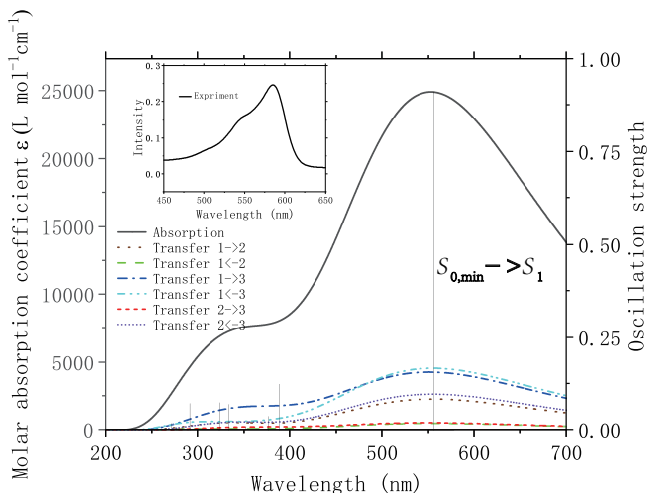


Figure 3: Charge-transfer spectrum. The solid black solid line is the normal absorption spectrum, and the dots or lines of other colors indicate the contribution to the absorption spectrum when electrons transfer between regions 1–3. Vertical lines correspond to the right axis, indicating the oscillator strength. The highest one vertical line corresponds to the $S_{0,min} \rightarrow S_1$ transition. The subgraph shows the absorption spectrum of mCherry measured in our experiment.

Charge-Transfer Spectrum. The absorption spectrum of the mCherry and the contribution of charge transfer between regions to the absorption spectrum are shown in Fig.3. According to the hole-electron distribution in Fig.2(a), there are no holes or electrons in Region 4; hence, we only consider charge transfer between Regions 1–3. The dark blue dot-dash line and the light blue double dot-dash line have the largest effect on the spectrum, representing the charge transfer between Regions 1 and 3, namely between the phenolate and imidazolinone rings. The brown dotted line and the purple short dotted line have a slightly less impact, representing the charge transfer from Region 1 and Region 3 to Region 2, i.e., the contribution to the absorption spectrum when the charges in the phenolate and imidazolinone rings move to the region in between them. Fig.3 clearly shows that the oscillator intensity corresponding to the $S_{0,min} \rightarrow S_1$ transition is the largest, and the contribution to the absorption spectrum is the largest, confirming our specula-

tion. The subfigure shows the mCherry absorption spectrum measured in our experimentally, and its trend is consistent with our calculation results. Combined with the consistent trend of the experimental and calculated results and the above conclusion that the hole-electron distribution does not change with the increase in the QM region, we conclude that our study can describe the mCherry transition mechanism.

Interfragment Charge Transfer. Fig.4 shows the specific electron transfer values between regions or heavy atoms. Combining Fig.3 and 4(a), it can be found that many electrons are transferred between Region 1 and Region 3, which also makes great contributions to the absorption spectrum. The more the number of electrons transferred, the greater the contribution to the absorption spectrum. With 1.157 electrons transferred within Region 1 and simultaneously 0.206 electrons moving within Region 3, it is conceivable that both parts also substantially contribute to the absorption spectrum. Overall, Region 1 lost 0.081 electrons, Region 3 lost 0.11 electrons, and instead, Region 2 obtained 0.181 electrons. Therefore, electrons generally move from phenolate and imidazolinone to the C16 atom between them. This conclusion is different from that of electron transfer obtained from observing the positive (negative) electron density difference centroid, in the case of which the electrons move purely from phenolate to imidazolinone.²⁷ The hole-electron distribution map directly shows the original distribution characteristics of holes and electrons without cancelation, which has certain advantages in investigating the intrinsic characteristics of electron excitation. Furthermore, if we judge the direction of electron transfer by referring to the hole centroid and the electron centroid, the result is consistent with that observed from the perspective of density difference.

The electron transfer between regions can be more intuitively understood from Fig.4(b), in which a large number of electrons are transferred into Region 2 (colored green), whereas very few atoms are transferred out of Region 2 (colored dark blue). The number of electrons transferred between Regions 1 and 3 is very close, both shown in orange. Region 3

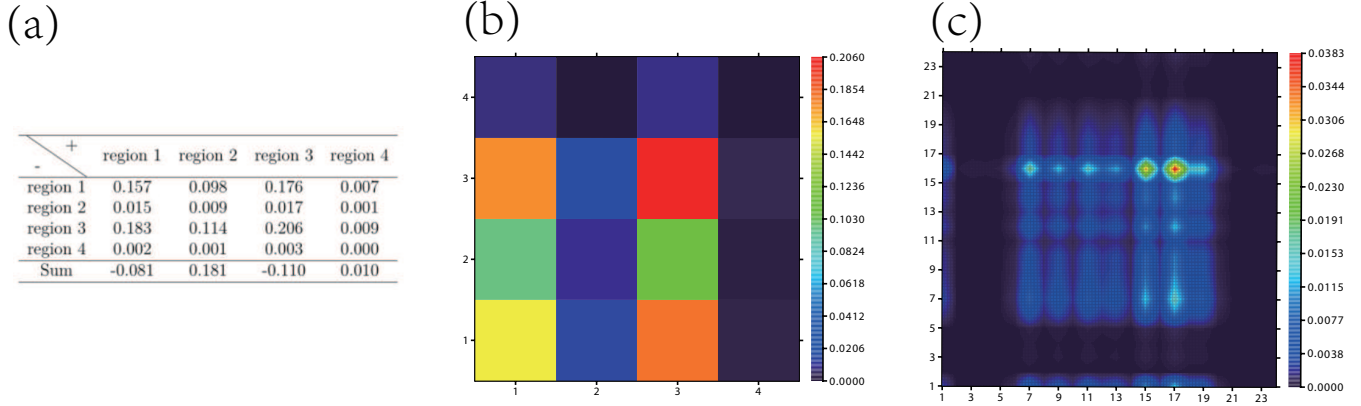


Figure 4: (a) Charge transfer between regions during $S_{0,min} \rightarrow S_1$; $-(+)$ represents the region where electrons are lost (obtained), and the last row represents the total change in the number of electrons. (b) The corresponding heat map. The horizontal (vertical) coordinates indicate the region of lost (obtained) electrons. (c) Heat map showing the charge transfer between heavy atoms. The horizontal (vertical) coordinates represent heavy atoms that have lost (obtained) electrons. The redder the color in (b) and (c), the more electrons are transferred.

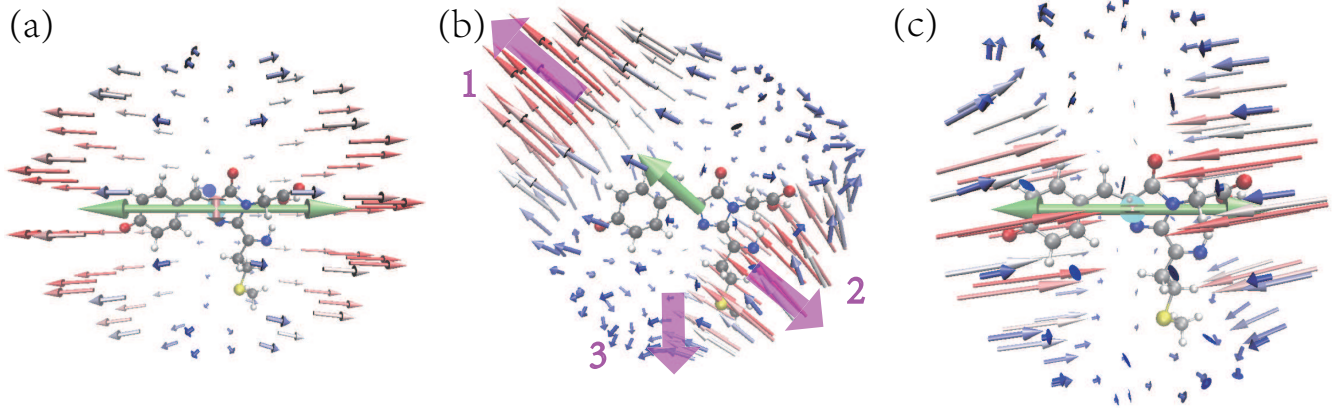


Figure 5: The polarization (a), first hyperpolarization (b), and second hyperpolarization (c) shown in unit spherical representation. The longer the arrow is, the redder it is, indicating that if outfields with unit strength are added from the molecular center to the direction, the greater the polarization, the first hyperpolarization and the second hyperpolarization will be. The shorter the arrow, the bluer it is, indicating the opposite meaning. In (a) and (c), the green double arrow, the orange double arrow (center) and the blue circle (center) represent the components in the x , y , z direction, respectively. In (b), the green arrow represents the overall orientation of the first hyperpolarizability, and the pink arrows are added for convenience.

has the highest number of redistributed electrons, shown in red. Additionally, if the four regions are not divided, the heat map of the direct study on charge transfer between heavy atoms, as shown in Fig.4(c), can be found from another perspective that electrons are concentrated in *C16* in Region 2, and the nearby *C15* and *C17* transfer an extra large number of electrons to *C16*. In contrast, the result of electron transfer is that *C16* is negatively charged, with the possibility of proton absorption, which is very similar to the blinking mechanism⁵⁶ in IrisFP. The blinking mechanism⁵⁷ of IrisFP is the thermally reversible photoinduced proton exchange between the methylene bridge of the chromophore and the surrounding residues. In particular, the chromophore of IrisFP acquired protons at exactly the same site as that of *C16* in the chromophore of mCherry. Therefore, it is possible for *C16* to absorb the proton and protonize the chromophore, resulting in photo-transformation of mCherry.

Linear and Nonlinear Optical Properties. Fig.5 displays the anisotropy of polarization, the first hyperpolarization, and the second hyperpolarization using unit spherical representation. In Fig.5(a) and Fig.5(c), the components in the *y* and *z* directions are negligible relative to the *x* direction. Thus, applying the external fields in the connection direction of the phenolate ring and the imidazolone ring can generate relatively large polarization and second hyperpolarization. In contrast, the polarization and second hyperpolarization are relatively negligible when the outer fields are perpendicular to the *x* direction. According to the electron transfer situation shown in Fig.4, the external field applied in *x* direction is in the same direction as the electron transfer, resulting in the largest influence on polarization or hyperpolarization. In contrast, the influence of the external field perpendicular to the electron transfer direction is negligible. As for Fig.5(b), the first hyperpolarization generated by outfields applied in direction 1 is larger and in the same direction as the outfields, but the first hyperpolarization generated by outfields applied in direction 2 is opposite to the outfields, whereas the first hyperpolariza-

tion generated by outfields applied in direction 3 is smaller and perpendicular to the outfields.

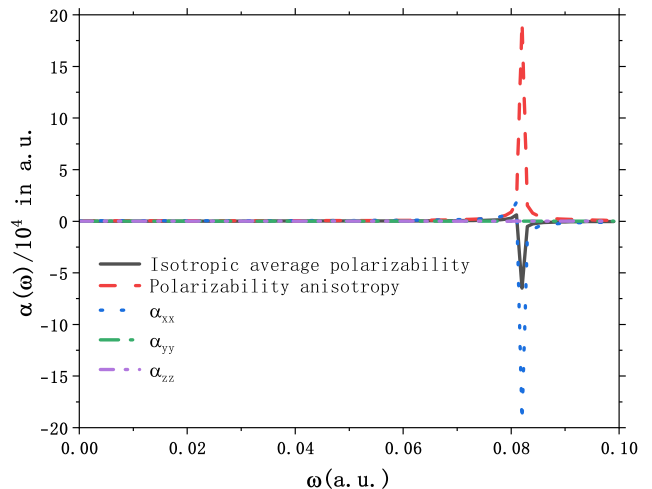


Figure 6: Polarizability (α) in different external fields (frequency ω). The solid black line is the isotropic average polarization, and the red dashed line is the polarizability anisotropy. The blue dot line, the green dot-dash line, and the purple double dotted line represent the polarization components in the *x*, *y*, and *z* directions, respectively.

Fig.6 studies the variation of the polarizability with the frequency of the outfield. It shows that when the external field frequency is 0.082 a.u. (about 556 nm), satisfying the $S_{0,min} \rightarrow S_1$ transition, the polarizability is mutated while the polarizabilities in all directions around the transition point obviously differ from each other. Specifically, the main reason is that the polarization of *x* direction undergoes a huge change while the polarizations of the *y* and *z* directions can be ignored in terms of both the absolute size and the degree of change. Moreover, the absolute value of anisotropic polarization (orange) is considerably higher than that of isotropic average polarization (black), and the polarization of mCherry presents significant anisotropy.

The scanning of the first hyperpolarizability as a function of the frequency of the field in Fig.7 demonstrates the excellent nonlinear optical characteristics of mCherry. The positive and negative signs of frequencies ω_1 and ω_2 have no physical significance. If the peak occurs

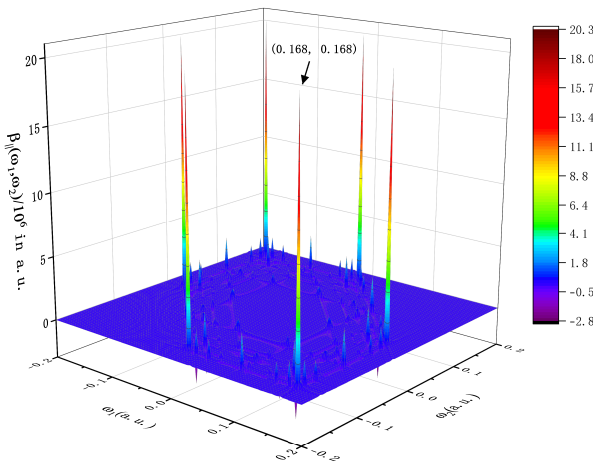


Figure 7: A scan of the first hyperpolarizability in the direction parallel to the dipole moment ($\beta_{||}$) as a function of the two external field frequencies (ω_1, ω_2). The color ranges from purple to red; the higher the second hyperpolarization, the redder the color.

when ω_1 and ω_2 symbols are the same, it corresponds to the combined frequency effect. In contrast, when the peaks with the opposite ω_1 and ω_2 symbols reflect the difference frequency effect. Specifically, the peak at $\omega_1 = \omega_2$ represents the second harmonic generation effect at the corresponding frequency; in the absence of any adjustment in these two fields, if the effect is optical rectification, the peak appears at $\omega_1 = -\omega_2$.^{58,59}

Abundant peaks appeared in our simulation, with six peaks far exceeding the others in height. Four of the six highest peaks correspond to ω_1 or ω_2 values of 0, reflecting a linear photoelectric effect, and can be used in fields such as electric-optical regulators. Two of the highest peaks satisfy $\omega_1 = \omega_2$ and generate second harmonics at their locations, which can be used in frequency multipliers and second-harmonic generation microscopy.^{37,60} Observing the external field frequencies corresponding to these six peaks, if the frequency of one field is 0, the other external field frequency size is 0.168 a.u. (271.2 nm); in contrast, when $\omega_1 = \omega_2$, both external field frequency sizes are 0.168 a.u. Using different calculation methods, the frequency and wavelength of the nonzero field at the peak will change but the trend of the first hyperpo-

larizability changing with outfields is similar.

CONCLUSIONS

Here, we investigate the transition mechanism of mCherry during the absorption process and its linear (nonlinear) optical properties. With Multiwfn software, we introduced the hole-electron analysis method to investigate the transition mechanism of mCherry. Based on the absorption spectra we simulated with the QMMM method is consistent with the trend we obtained experimentally, and that expanding the QM region does not affect the hole-electron distribution, i.e., the electron transfer is concentrated in the chromophore, we judge our simulation and analysis are reliable. According to the charge transfer spectrum, a substantial charge transfer occurred between phenolate and imidazolinone, which considerably contributed to the absorption spectrum. Interestingly, the electrons converge overall towards the C16 atom between the phenolate ring and the imidazolinone ring during absorption, which different from the observed direction of electron movement along phenolate to imidazolinone from the perspective of the density difference.²⁷ However, from the perspectives of the hole centroid and the electron centroid, the electron transfer direction was the same as the density difference perspective. Similar to the blinking mechanism^{56,57} of IrisFP, the chromophore of mCherry may also absorb proton at C16 after excitation, thus achieving protonation and resulting photoconversion of mCherry.

In addition to investigating the transition mechanism of mCherry during the absorption process, we further analyzed its linear and nonlinear optical properties in different external fields. We utilized the unit spherical representation method to study the anisotropy of polarization, first hyperpolarization, and second hyperpolarization. Our results show that the polarizability and second hyperpolarizability are considerably larger in the phenolate and imidazolinone connection direction than when perpendicular to this direction. In connection with the previous analysis of the transition mecha-

nism, this phenomenon is due to electrons moving mainly in this direction. Then, we study the polarizability in the outer field at different frequencies, and find that the polarizability is mutated in the connection direction of the phenolate loop and the imidazolinone loop when the outer field satisfies the $S_{0,min} \rightarrow S_1$ transition. Finally, we investigated the variation of the first hyperpolarizability in two different fields and plotted the scan. Our simulation results show that mCherry can produce a linear photoelectric effect (the nonzero external wavelength is 271.2 nm) or second harmonic wave (both external field wavelengths are 271.2 nm) by adjusting the appropriate external fields, which has great application value in the electro-optic regulator, frequency multiplier, and second-harmonic imaging microscopy.³⁷

Given the similarity of RFPs, we suggest that the transition mechanism and optical properties of mCherry can be extricated to other RFPs. The analytical techniques, such as hole-electron analysis and unit spherical representation method used herein, can also be applied to other FPs. At present, there are few detailed analyses of how electrons are transferred in the photoinduced reaction of FPs. The hole-electron analysis is more intuitive and detailed than the electron density method^{61,62} commonly used to analyze FPs and can be used to study electron transfer in various photoinduced reactions. Finally, we believe that our study can serve as a reference for mCherry and other fluorescence protein-related experiments and simulations.

Acknowledgement The authors thank financial support from the National Natural Science Foundation of China (12204040).

References

- (1) Mishin, A. S.; Belousov, V. V.; Solntsev, K. M.; Lukyanov, K. A. Novel uses of fluorescent proteins. *Current Opinion in Chemical Biology* **2015**, *27*, 1–9, Molecular imaging.
- (2) Zhang, J.; Campbell, R. E.; Ting, A. Y.; Tsien, R. Y. Creating new fluorescent probes for cell biology. *Nature Reviews Molecular Cell Biology* **2002**, *3*, 906–918.
- (3) Mukherjee, S.; Jimenez, R. Photophysical Engineering of Fluorescent Proteins: Accomplishments and Challenges of Physical Chemistry Strategies. *The Journal of Physical Chemistry B* **2022**, *126*, 735–750, PMID: 35075898.
- (4) Dean, K. M.; Palmer, A. E. Advances in fluorescence labeling strategies for dynamic cellular imaging. *Nature Chemical Biology* **2014**, *10*, 512–523.
- (5) Montero Llopis, P.; Senft, R. A.; Ross-Elliott, T. J.; Stephansky, R.; Keeley, D. P.; Koshar, P.; Marqués, G.; Gao, Y.-S.; Carlson, B. R.; Pengo, T.; Sanders, M. A.; Cameron, L. A.; Itano, M. S. Best practices and tools for reporting reproducible fluorescence microscopy methods. *Nature Methods* **2021**, *18*, 1463–1476.
- (6) Koch, M.; Symvoulidis, P.; Ntziachristos, V. Tackling standardization in fluorescence molecular imaging. *Nature Photonics* **2018**, *12*, 505–515.
- (7) Bando, Y.; Sakamoto, M.; Kim, S.; Ayzenshtat, I.; Yuste, R. Comparative Evaluation of Genetically Encoded Voltage Indicators. *Cell Reports* **2019**, *26*, 802–813.e4.
- (8) Mo, H.-M.; Xu, Y.; Yu, X.-W. Improved Soluble Expression and Catalytic Activity of a Thermostable Esterase Using a High-Throughput Screening System Based on a Split-GFP Assembly. *Journal of Agricultural and Food Chemistry* **2018**, *66*, 12756–12764, PMID: 30411620.
- (9) Ranjit, S.; Lanzanò, L.; Libby, A. E.; Gratton, E.; Levi, M. Advances in fluorescence microscopy techniques to study kidney function. *Nature Reviews Nephrology* **2021**, *17*, 128–144.

- (10) Duwé, S.; Dedecker, P. Optimizing the fluorescent protein toolbox and its use. *Current Opinion in Biotechnology* **2019**, *58*, 183–191, Systems Biology • Nanobiotechnology.
- (11) Wang, S.; Ren, W. X.; Hou, J.-T.; Won, M.; An, J.; Chen, X.; Shu, J.; Kim, J. S. Fluorescence imaging of pathophysiological microenvironments. *Chem. Soc. Rev.* **2021**, *50*, 8887–8902.
- (12) Zhou, J.; del Rosal, B.; Jaque, D.; Uchiyama, S.; Jin, D. Advances and challenges for fluorescence nanothermometry. *Nature Methods* **2020**, *17*, 967–980.
- (13) Mieog, J. S. D.; Achterberg, F. B.; Zliti, A.; Hutteman, M.; Burggraaf, J.; Swijnenburg, R.-J.; Gioux, S.; Vahrmeijer, A. L. Fundamentals and developments in fluorescence-guided cancer surgery. *Nature Reviews Clinical Oncology* **2022**, *19*, 9–22.
- (14) Coelho, S.; Poland, S. P.; Devauges, V.; Ameer-Beg, S. M. Adaptive optics for a time-resolved Förster resonance energy transfer (FRET) and fluorescence lifetime imaging microscopy (FLIM) in vivo. *Opt. Lett.* **2020**, *45*, 2732–2735.
- (15) Acharya, A.; Bogdanov, A. M.; Grigorenko, B. L.; Bravaya, K. B.; Nemukhin, A. V.; Lukyanov, K. A.; Krylov, A. I. Photoinduced Chemistry in Fluorescent Proteins: Curse or Blessing? *Chemical Reviews* **2017**, *117*, 758–795, PMID: 27754659.
- (16) Coquelle, N. et al. Chromophore twisting in the excited state of a photoswitchable fluorescent protein captured by time-resolved serial femtosecond crystallography. *Nature Chemistry* **2018**, *10*, 31–37.
- (17) Adam, V.; Berardozi, R.; Byrdin, M.; Bourgeois, D. Phototransformable fluorescent proteins: Future challenges. *Current opinion in chemical biology* **2014**, *20*, 92–102.
- (18) Nienhaus, K.; Ulrich Nienhaus, G. Fluorescent proteins for live-cell imaging with super-resolution. *Chem. Soc. Rev.* **2014**, *43*, 1088–1106.
- (19) Sigal, Y. M.; Zhou, R.; Zhuang, X. Visualizing and discovering cellular structures with super-resolution microscopy. *Science* **2018**, *361*, 880–887.
- (20) Ma, T.; Li, T.; Zhou, L.; Ma, X.; Yin, J.; Jiang, X. Dynamic wrinkling pattern exhibiting tunable fluorescence for anticounterfeiting applications. *Nature Communications* **2020**, *11*, 1811.
- (21) Qi, Q.; Li, C.; Liu, X.; Jiang, S.; Xu, Z.; Lee, R.; Zhu, M.; Xu, B.; Tian, W. Solid-State Photoinduced Luminescence Switch for Advanced Anticounterfeiting and Super-Resolution Imaging Applications. *Journal of the American Chemical Society* **2017**, *139*, 16036–16039, PMID: 29045132.
- (22) Zuo, M.; Qian, W.; Li, T.; Hu, X.-Y.; Jiang, J.; Wang, L. Full-Color Tunable Fluorescent and Chemiluminescent Supramolecular Nanoparticles for Anti-counterfeiting Inks. *ACS Applied Materials & Interfaces* **2018**, *10*, 39214–39221.
- (23) Gao, Z.; Han, Y.; Wang, F. Cooperative supramolecular polymers with anthracene–endoperoxide photo-switching for fluorescent anti-counterfeiting. *Nature Communications* **2018**, *9*, 3977.
- (24) Liu, Y. et al. Inkjet-printed unclonable quantum dot fluorescent anti-counterfeiting labels with artificial intelligence authentication. *Nature Communications* **2019**, *10*, 2409.
- (25) Duan, C.; Won, M.; Verwilt, P.; Xu, J.; Kim, H. S.; Zeng, L.; Kim, J. S. In Vivo Imaging of Endogenously Produced HClO in Zebrafish and Mice Using a Bright, Photostable Ratiometric Fluorescent Probe. *Analytical Chemistry* **2019**, *91*, 4172–4178, PMID: 30784257.

- (26) Kannan, M.; Vasan, G.; Huang, C.; Haziza, S.; Li, J. Z.; Inan, H.; Schnitzer, M. J.; Pieribone, V. A. Fast, in vivo voltage imaging using a red fluorescent indicator. *Nature methods* **2018**, *15*, 1108–1116.
- (27) Khrenova, M. G.; Mulashkin, F. D.; Nemukhin, A. V. Modeling Spectral Tuning in Red Fluorescent Proteins Using the Dipole Moment Variation upon Excitation. *Journal of Chemical Information and Modeling* **2021**, *61*, 5125–5132, PMID: 34601882.
- (28) Shaner, N. C.; Campbell, R. E.; Steinbach, P. A.; Giepmans, B. N. G.; Palmer, A. E.; Tsien, R. Y. Improved monomeric red, orange and yellow fluorescent proteins derived from *Discosoma* sp. red fluorescent protein. *Nature Biotechnology* **2004**, *22*, 1567–1572.
- (29) Matz, M. V.; Fradkov, A. F.; Labas, Y. A.; Savitsky, A. P.; Zaraisky, A. G.; Markelov, M. L.; Lukyanov, S. A. Fluorescent proteins from nonbioluminescent Anthozoa species. *Nature Biotechnology* **1999**, *17*, 969–973.
- (30) Yarbrough, D.; Wachter, R. M.; Kallio, K.; Matz, M. V.; Remington, S. J. Refined crystal structure of DsRed, a red fluorescent protein from coral, at 2.0-Å resolution. *Proceedings of the National Academy of Sciences* **2001**, *98*, 462–467.
- (31) Campbell, R. E.; Tour, O.; Palmer, A. E.; Steinbach, P. A.; Baird, G. S.; Zacharias, D. A.; Tsien, R. Y. A monomeric red fluorescent protein. *Proceedings of the National Academy of Sciences* **2002**, *99*, 7877–7882.
- (32) Merzlyak, E. M.; Goedhart, J.; Shcherbo, D.; Bulina, M. E.; Shcheglov, A. S.; Fradkov, A. F.; Gaintzeva, A.; Lukyanov, K. A.; Lukyanov, S.; Gadella, T. W. J.; Chudakov, D. M. Bright monomeric red fluorescent protein with an extended fluorescence lifetime. *Nature Methods* **2007**, *4*, 555–557.
- (33) Shaner, N. C.; Steinbach, P. A.; Tsien, R. Y. A guide to choosing fluorescent proteins. *Nature Methods* **2005**, *2*, 905–909.
- (34) Chapagain, P. P.; Regmi, C. K.; Castillo, W. Fluorescent protein barrel fluctuations and oxygen diffusion pathways in mCherry. *The Journal of Chemical Physics* **2011**, *135*, 235101.
- (35) Mukherjee, S.; Manna, P.; Hung, S.-T.; Vietmeyer, F.; Friis, P.; Palmer, A.; Jimenez, R. Directed evolution of a bright variant of mCherry: Suppression of non-radiative decay by fluorescence lifetime selections. *ChemRxiv* **2022**,
- (36) Baird, G. S.; Zacharias, D. A.; Tsien, R. Y. Biochemistry, mutagenesis, and oligomerization of DsRed, a red fluorescent protein from coral. *Proceedings of the National Academy of Sciences* **2000**, *97*, 11984–11989.
- (37) De Meulenaere, E.; Nguyen Bich, N.; de Wergifosse, M.; Van Hecke, K.; Van Meervelt, L.; Vanderleyden, J.; Champagne, B.; Clays, K. Improving the Second-Order Nonlinear Optical Response of Fluorescent Proteins: The Symmetry Argument. *Journal of the American Chemical Society* **2013**, *135*, 4061–4069, PMID: 23406416.
- (38) Lu, T.; Chen, F. Multiwfn: A multifunctional wavefunction analyzer. *Journal of Computational Chemistry* **2012**, *33*, 580–592.
- (39) Liu, Z.; Lu, T.; Chen, Q. An sp-hybridized all-carboatomic ring, cyclo[18]carbon: Bonding character, electron delocalization, and aromaticity. *Carbon* **2020**, *165*, 468–475.
- (40) Liu, Z.; Wang, X.; Lu, T.; Yuan, A.; Yan, X. Potential optical molecular switch: Lithium@cyclo[18]carbon complex transforming between two stable configurations. *Carbon* **2022**, *187*, 78–85.

- (41) Lu, T. Multiwfn Manual, Version 3.8(dev), Section 3.21.8. *available at: <http://sobereva.com/multiwfn/>* . (Accessed 12 April 2023).
- (42) Sasagane, K.; Aiga, F.; Itoh, R. Higher-order response theory based on the quasienergy derivatives: The derivation of the frequency-dependent polarizabilities and hyperpolarizabilities. *The Journal of Chemical Physics* **1993**, *99*, 3738–3778.
- (43) Tuer, A.; Krouglov, S.; Cisek, R.; Tokarz, D.; Barzda, V. Three-dimensional visualization of the first hyperpolarizability tensor. *Journal of Computational Chemistry* **2011**, *32*, 1128–1134.
- (44) Wang, X.; Liu, Z.; Yan, X.; Lu, T.; Wang, H.; Xiong, W.; Zhao, M. Photophysical properties and optical nonlinearity of cyclo[18]carbon (C18) precursors, C18–(CO)_n (n = 2, 4, and 6): focusing on the effect of the carbonyl groups. *Phys. Chem. Chem. Phys.* **2022**, *24*, 7466–7473.
- (45) Neese, F. The ORCA program system. *WIREs Computational Molecular Science* **2012**, *2*, 73–78.
- (46) Shu, X.; Shaner, N. C.; Yarbrough, C. A.; Tsieng, R. Y.; Remington, S. J. Novel Chromophores and Buried Charges Control Color in mFruits. *Biochemistry* **2006**, *45*, 9639–9647, PMID: 16893165.
- (47) Humphrey, W.; Dalke, A.; Schulten, K. VMD: Visual molecular dynamics. *Journal of Molecular Graphics* **1996**, *14*, 33–38.
- (48) Hanwell, M. D.; Curtis, D. E.; Lonie, D. C.; Vandermeersch, T.; Zurek, E.; Hutchison, G. R. Avogadro: an advanced semantic chemical editor, visualization, and analysis platform. *Journal of Cheminformatics* **2012**, *4*, 17.
- (49) Olsen, S.; McKenzie, R. H. A diabatic three-state representation of photoisomerization in the green fluorescent protein chromophore. *The Journal of Chemical Physics* **2009**, *130*, 184302.
- (50) List, N. H.; Jones, C. M.; Martínez, T. J. Internal conversion of the anionic GFP chromophore: in and out of the I-twisted S1/S0 conical intersection seam. *Chem. Sci.* **2022**, *13*, 373–385.
- (51) Lu, T. Multiwfn Manual, Version 3.8(dev), Section 3.200.7. *available at: <http://sobereva.com/multiwfn/>* . (Accessed 12 April 2023).
- (52) Brink, J. Murray, and P. Politzer. *J. Chem. Phys* **1993**, *98*, 4305.
- (53) Liu, Z.; Lu, T.; Yuan, A.; Wang, X.; Chen, Q.; Yan, X. Remarkable Size Effect on Photophysical and Nonlinear Optical Properties of All-Carboatomic Rings, Cyclo[18]carbon and Its Analogues. *Chemistry – An Asian Journal* **2021**, *16*, 2267–2271.
- (54) Hao, H.; ho Tam, L.; Lu, Y.; Lau, D. An atomistic study on the mechanical behavior of bamboo cell wall constituents. *Composites Part B: Engineering* **2018**, *151*, 222–231.
- (55) Hilborn, R. C. Einstein coefficients, cross sections, f values, dipole moments, and all that. *American Journal of Physics* **1982**, *50*, 982–986.
- (56) Roy, A.; Field, M. J.; Adam, V.; Bourgeois, D. The Nature of Transient Dark States in a Photoactivatable Fluorescent Protein. *Journal of the American Chemical Society* **2011**, *133*, 18586–18589, PMID: 22039963.
- (57) Adam, V.; Berardozi, R.; Byrdin, M.; Bourgeois, D. Phototransformable fluorescent proteins: Future challenges. *Current Opinion in Chemical Biology* **2014**, *20*, 92–102, Molecular imaging.
- (58) He, Y.-Y.; Chen, J.; Zheng, X.-L.; Xu, X.; Li, W.-Q.; Yang, L.; Tian, W. Q. Spiral

Graphene Nanoribbons with Azulene Defects as Potential Nonlinear Optical Materials. *ACS Applied Nano Materials* **2019**, *2*, 1648–1654.

- (59) Lu, T. Multiwfn Manual, Version 3.8(dev), Section 4.200.8.1. *available at: <http://sobereva.com/multiwfn/>* . (Accessed 12 April 2023).
- (60) He, H.; Zhou, M.; Qiao, T.; Lai, H. M.; Ran, Q.; Ren, Y.-X.; Ko, H.; Zheng, C.; Tsia, K. K.; Wong, K. K. Y. 890-nm-excited SHG and fluorescence imaging enabled by an all-fiber mode-locked laser. *Opt. Lett.* **2022**, *47*, 2710–2713.
- (61) Nasu, Y.; Shen, Y.; Kramer, L.; Campbell, R. E. Structure- and mechanism-guided design of single fluorescent protein-based biosensors. *Nature Chemical Biology* **2021**, *17*, 509–518.
- (62) Trachman, R. J.; Autour, A.; Jeng, S. C. Y.; Abdolazadeh, A.; Andreoni, A.; Cojocaru, R.; Garipov, R.; Dolgosheina, E. V.; Knutson, J. R.; Ryckelynck, M.; Unrau, P. J.; Ferré-D’Amaré, A. R. Structure and functional reselection of the Mango-III fluorogenic RNA aptamer. *Nature Chemical Biology* **2019**, *15*, 472–479.